JMEPEG (2013) 22:1816–1825
DOI: 10.1007/s11665-013-0509-z

1059-9495/$19.00

Evaluation of Flow Fields and Orientation Effects Around Ring Geometries During Quenching

Andrew L. Banka, B.L. Ferguson, and D.Scott MacKenzie

(Submitted June 18, 2012; in revised form September 11, 2012; published online March 5, 2013)

The orientation in which parts are held during the quenching operation can have a strong effect on the overall success of heat treating. Certain orientations can result in significantly greater distortion than other orientations, even when high-quality quenchants are used. In this study, various simple, rolled ring geometries are examined at two different orientations to quenchant flow using computational fluid dynamics with the software program AZORE®. These parts were examined singly without the influence of other parts in close proximity. Three rolled ring geometries were examined, using the same outside diameter, while the inside diameter was varied. These flow fields will be used for understanding the likely distortion occurring during quenching.

Keywords CFD, cracking, FEA, heat-treatment simulation, quenching, ring

1. Introduction

Rolled rings are used in many applications such as wind turbine bearings (yaw and pitch), jet engine bearings, the oil and gas industry, mining, and others wherever a strong, uniform forged structure is required. The high tangential strength and toughness make forged rings the preferred choice for high torque applications. Alloys used in the manufacture of rolled rings can be not only carbon and alloy steels, but also stainless steels, and nonferrous alloys like aluminum, copper, and nickel-based superalloys.

The manufacture of rolled rings starts with hot upsetting of a billet, followed by punching and piercing to form a torus or donut shape. The resulting preform is now ready for the ring-rolling operation. The preform is slipped over a smaller diameter idler roll. A drive roll is moved into position against the preform. The ring rolling process begins with idler roll applying pressure to the preform against the drive roll. The ring diameter is increased by continuous movement of the idler roll toward the drive roll to reduce the ring radial thickness. The height of the rolled ring is controlled by axial pinch rolls. This process is continued until the required dimensions are achieved. Once the hot working of the ring is completed, it can then be heat treated and machined to the final dimensions.

During the heat-treatment process, especially with high hardenable alloys such as AISI 4140 or 4150, quench cracking can occur. Cracking is often associated with a forging defect. However, in many cases, no such defect is present, and the crack is actually generated during quenching. The morphology of the cracking can vary. Cracking can be radial cracking; top or bottom surface circumferential cracking, or circumferential cracking along the inside or outside diameter, as shown in Fig. 1. Since each of these cracking morphologies suggests the presence of a different stress field, an investigation was conducted to understand the relationships that geometry and orientation exhibit in the flow field and heat transfer around the parts, with the intent of understanding the cause of the different types of cracking mechanisms. The expected stress fields for the different cracking mechanisms are listed in Table 1.

Heat treatment of the rings follows normal practice of austenization, quenching, and tempering. Adequate time is allowed for the parts to fully soak at temperature, and then the parts are quenched in water, polymer quenchants, or in oil.

For the present study, three representative rolled rings with varying wall thickness are considered, and the stresses that occur during quenching are estimated using a combination of computational fluid dynamics (CFD) and FEA analyses. In order to simplify the process, the rings are considered individually, without including the effects of adjacent parts, fixturing, or base trays. Likewise, the rings are placed in an idealized, uniform flow field. The flow around the parts and the associated convective heat fluxes were determined through CFD modeling. Those heat fluxes were then applied as boundary conditions to an FEA model, which was used to predict the cooling rate, phase transformations, stresses, and distortion.

2. Modeling

For this study, the methods of analysis used included both CFD and thermal/stress analyses using the finite element method. The sizes of rings modeled are shown in Table 2.

This article is an invited paper selected from presentations at the 26th ASM Heat Treating Society Conference, held October 31 through November 2, 2011, in Cincinnati, Ohio, and has been expanded from the original presentation.

Andrew L. Banka, Airflow Sciences Corporation, 12190 Hubbard Street, Livonia, MI 48150-1737; **B.L. Ferguson**, Deformation Control Technology, Inc., 7261 Engle Road, Suite 105, Cleveland, OH 44130; and **D. Scott MacKenzie**, Houghton International, Inc., Madison and Van Buren Aves, Valley Forge, PA 19482. Contact e-mails: abanka@airflowsciences.com, lynn.ferguson@deformationcontrol.com, and smackenzie@houghtonintl.com.

Fig. 1 Example of quench cracking of large rolled rings, with cracking emanating from the inner bore

Table 1 Expected stress fields for observed cracking morphologies

Cracking mechanism (assuming horizontal orientation)	Likely stress field
Radial cracking	High hoop stress field
Top or bottom circumferential cracking	High radial stress field
Inner or outer diameter circumferential cracking	High axial stress field

Table 2 Sizes of rings used in this investigation

Ring	Outer diameter, mm	Wall, mm	Inner diameter, mm	Height, mm
Ring 1	610	127	356	127
Ring 2	610	64	482	127
Ring 3	610	25	560	127

2.1 Computational Fluid Dynamics

The flow simulations were performed using the Azore® CFD code (Ref 1), a general purpose software package providing a control-volume-based numerical algorithm utilizing a state-of-the-art solution algorithm (Ref 2). The domain for the CFD simulations of the rolled rings was a cube, 1524 mm on each side, which provided sufficient distance to avoid influence from the model boundaries. A single, computational grid was created for each of the three rolled rings, with the different flow conditions being achieved by changing the boundary conditions on the model domain. Figure 2 provides an overall view of the grid used for Ring 2, and shows a close-up of the grid detail close in to the ring. A mapped mesh was used on all faces of the rings, with 288 cells around the periphery of the ring, 51 cells along the 5″ height, and 43, 15, and 7 cells in the radial direction for the three rings. A two-cell boundary layer mesh was applied to all faces of the rings to provide good calculation of near-surface gradients. The size of the first cell was 1.27 mm for all cases. Owing to differences in the sizes of the rings, the total grid count varied slightly, ranging from 3.6 to 3.9 million cells.

All the flow simulations were run using constant fluid properties of water with an inlet velocity of 0.25 m/s. The ring surface temperature was held 100 °C above the fluid inlet temperature. Since the relevant output from the CFD simulation is the heat-transfer coefficient (rather than the heat flux rate), the use of a constant surface temperature essentially assumes that the change in quenchant properties with temperature has a minor effect on the overall results.

Constant pressure was assumed for the opposing boundary, while the four side boundaries were assumed to be planes of symmetry. Turbulence was simulated using the standard k-ε model, and standard law of the wall (Ref 3) was used to treat the laminar sub-layer near the ring surfaces. y^* values, which define the nondimensional distance from the wall to the first near-wall grid point, were in the range of 10-100 for all cases. While the y^* values in some areas fell below the threshold value of 11.5, those regions were confined to small areas of the vertical orientation models. The low y^* values indicated that the near-surface grid length scale was too fine in these areas, which significantly reduces the accuracy of the heat transfer and skin friction predictions in these areas. Heat-transfer coefficients reported later are based on the calculated heat flux values and the temperature differential between the part and the quenchant.

2.2 Heat-Treatment Analyses

Analysis of the heat treatment of the rings was done using the DANTE® software for predicting phase transformations, residual stress, and distortion of steel parts due to quench hardening (Ref 4). The flow fields predicted by the CFD analyses were used to adjust the heat-transfer coefficient datasets assigned to the ring surfaces. Mapping was required to translate CFD model results for use in the DANTE models. This involved using the local heat-transfer data calculated in the static CFD models and mapping these values to surface mesh in the finite element models. Mechanical, thermal, and phase transformation data in the DANTE database for AISI 4340 steel were used for the simulations.

The initial ring temperature in the DANTE models is 20 °C. The rings are heated to 900 °C, transferred through air to the quench tank, and quenched in oil. Surface heat transfer is active in each step. The rings are assumed to be stress free before

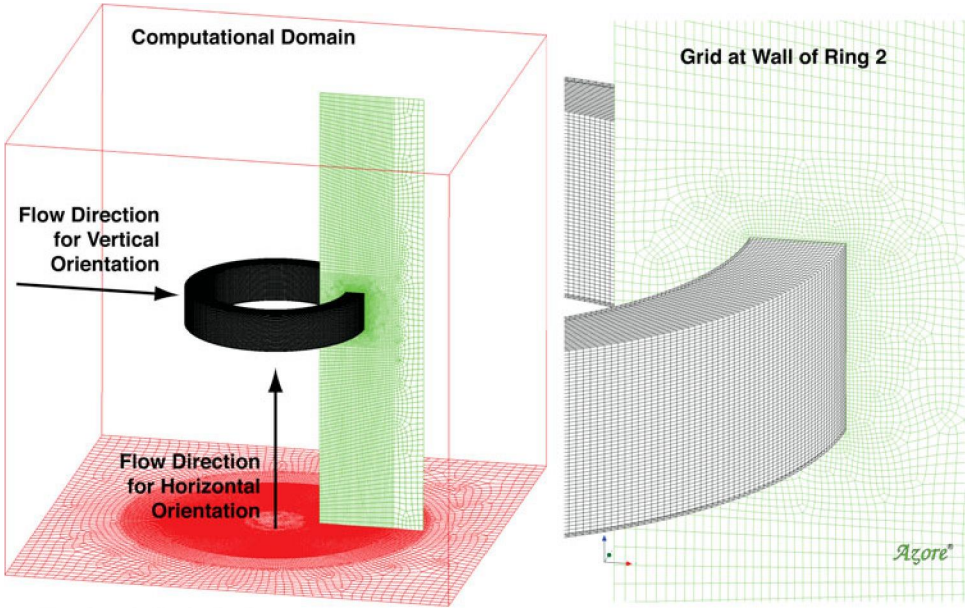

Fig. 2 Showing the computational domain used in this investigation and the grid in proximity to the wall of the rolled ring

heating, and the heating rate is low enough that no distortion occurs during heating.

For cases where the ring was positioned horizontally (vertical ring axis), boundary conditions were symmetric around the rings and 2D, axisymmetric models were developed, and executed. For cases where the ring was vertical, 3D models were required. Values for local average heat-transfer coefficients were assigned in the heat-treated models based on the average local heat fluxes calculated in the CFD models.

3. Results for Horizontal Ring Orientation

Figure 3 shows the total velocity for the horizontal ring orientations, with the general flow pattern being from bottom to top of the figure. The flow field is radially symmetric and can be defined by a single plane through the ring axis. In each case, there is a stagnation zone on the bottom surface of the ring, and a wake zone on the top surface. While the flow appears to be uniformly low in the wake regions for Rings 2 and 3, the presence of a second color band above the top surface of Ring 1 suggests a more complex flow pattern for that case.

As the flow passes the lower edge of the rings, it separates from the surface, leaving a low-velocity region on the lower portions of the ID and OD surfaces. Ring 3 shows reattachment of the flow to the ID and OD surfaces, while the other two rings show reattachment only on the ID surfaces. Acceleration of the flow around the thicker rings is greater than for the thinner rings.

Surface heat-transfer coefficients are shown in Fig. 4 for the horizontal ring cases. Figure 5 shows in more detail the line plots of surface heat-transfer coefficients across each surface, with the vertical ID and OD surface data in part (a) and the horizontal bottom and top surface data in part (b). All cases show higher heat transfer on the lower surfaces and on the lower edges. On the upper surface, Rings 2 and 3 show uniformly low heat-transfer coefficients on the upper surface, while Ring 1 shows a more complex behavior that results from the more complex flow predicted in the wake region for that case. All cases show heat-transfer coefficients on the ID surfaces that decrease from a high value on the lower edge to a lower value on the upper edge. The OD surfaces show a more striking difference between the cases. For Ring 1, the heat-transfer coefficient is low toward the lower edge and increases toward the top. Ring 2 shows a nearly constant heat-transfer coefficient along the OD surface, while the heat-transfer coefficient for Ring 3 is high near the bottom edge and decreases toward the upper surface.

Radial displacement predictions are shown in the contour plots of Fig. 6. The displacements are magnified in these cross sectional plots, and so they are easier to observe.

- The thin Ring 3 is predicted to hourglass, with the ID mid-height region shrinking about 60 μm, the bottom section of the ID growing 45 μm, and the top section of the ID growing 25 μm.
- Ring 2 is predicted to bulge on both the ID and OD surfaces at mid-height, with the ID shrinking about 300 μm and the OD growing about 400 μm. The cross section is shown to also taper or cock, with the top shrinking about 150 μm and the bottom growing about 400 μm.
- Ring 1 is predicted to bulge slightly on all surfaces. There is overall a radial growth, with the top growing about 120 μm and the bottom growing about 350 μm. These values are only approximations as the figure shows that the corners move different amounts.

Axial stress predictions are shown in Fig. 7 for rings quenched in the horizontal orientation. Again, the shape change is magnified by 10 times for easier discernment. Comparison of ID and OD surface stresses for the three rings is interesting. The thin ring, Ring 3, has a maximum final axial surface stress of ~190 MPa, and it is located at about two-thirds of the height of the ring. Ring 2 has the highest surface tension, and it is maximum at roughly mid-height, with the ID being at 600 MPa

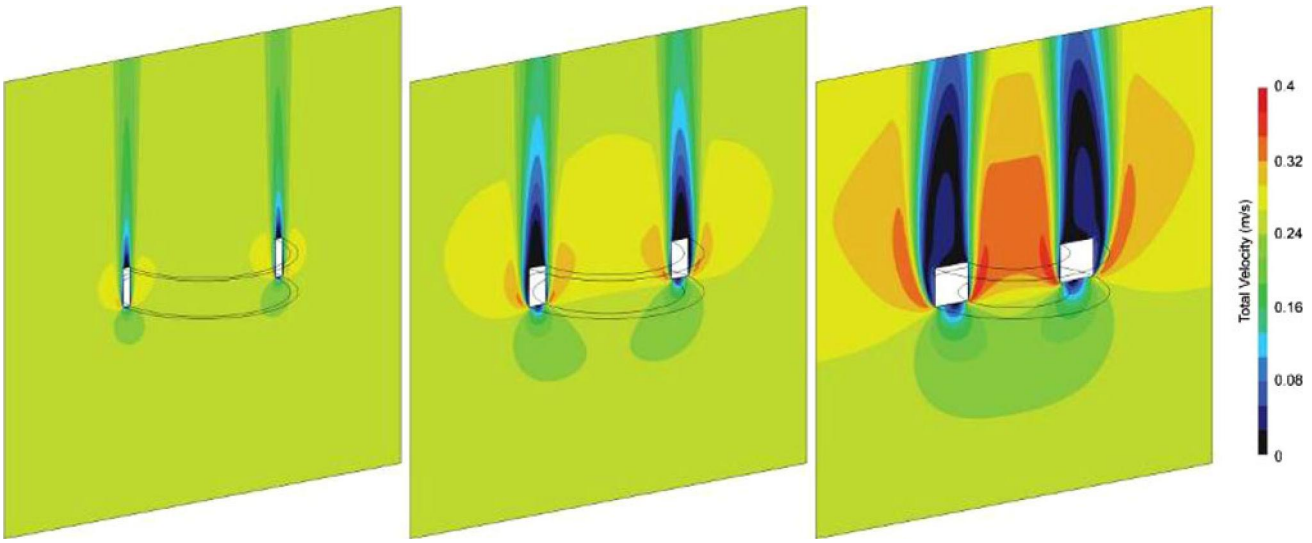

Fig. 3 Flow fields surrounding the three horizontal rings with vertical flow. Ring 3 is shown at left, Ring 2 is in the middle, and Ring 1 is at the right (Color figure online)

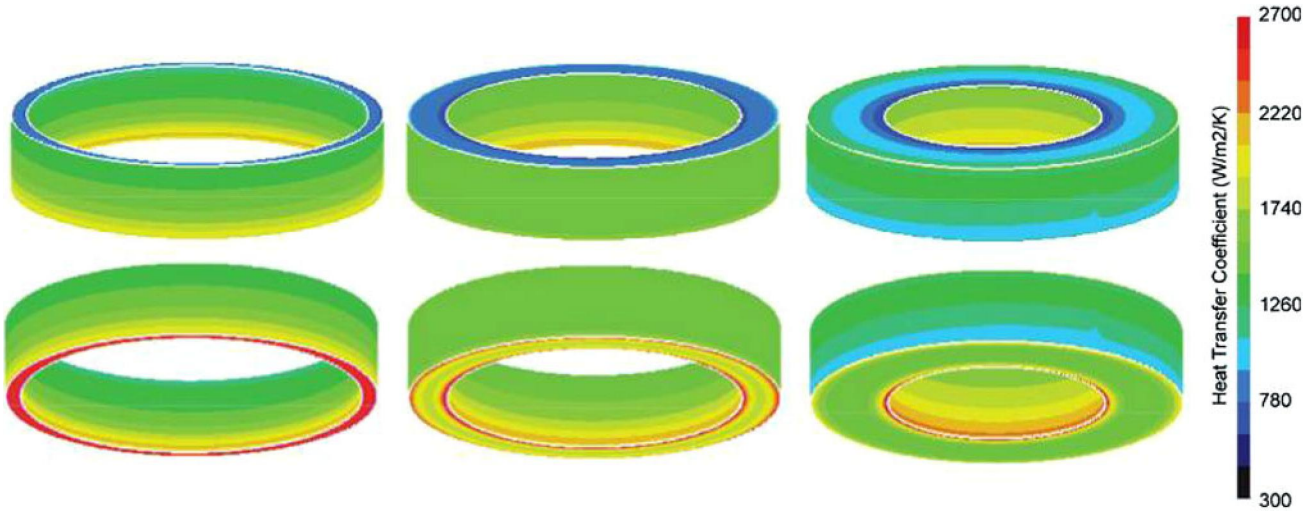

Fig. 4 Heat-transfer coefficients for horizontal rings. Ring 3 is on the left, Ring 2 is in the middle, and Ring 1 is on the right (Color figure online)

and the OD at 500 MPa. Ring 3 also has surface axial tension on the ID, but the values are lower at about 250-300 MPa. However, just inside the ID surface at mid-height is a pocket of residual axial tension of magnitude about 550 MPa.

4. Results for Vertical Ring Orientation

The flow field around the vertically oriented rings during quenching is more complicated as the flow is truly three dimensional in nature. Figure 8 shows velocities in the two symmetry planes for this orientation, with the top row showing the vertical plane parallel to each ring axis and the bottom row showing the cut plane perpendicular to each ring axis. There is a great deal of similarity between the three rings. The main features include a stagnation zone near the bottom, higher velocities around the sides of the OD, and a wake region above the ring. The flow is generally low on the inside of the ring.

The distribution of heat-transfer coefficients for the vertical cases is shown in Fig. 9, and it reflects the more complex flow patterns around the rings. For all three rings, the respective heat-transfer coefficient is fairly constant over the lower half of the rings, with the exception of the ID surface, which shows lower heat-transfer coefficients because of the lower stagnant flow in this region. Even though it is lower, the heat-transfer coefficient is fairly constant on the lower half of the ID surface. On the upper half of the ring, there is much more variation, primarily on the OD and ID surfaces. On the ID surface, flow that separated off of the lower portion of the ring has expanded into the open area of the ring, and impinges on the upper portion of the ID, resulting in higher heat-transfer coefficients near the sides and lower values in the face center. On the OD surface, the very top of the ring is in a wake region and has low heat-transfer rates. In more outboard regions, the flow wraps around the edge of the ring after passing over the sides of the ring, resulting again in higher heat transfer toward the edges of the ring, and lower values in the face center.

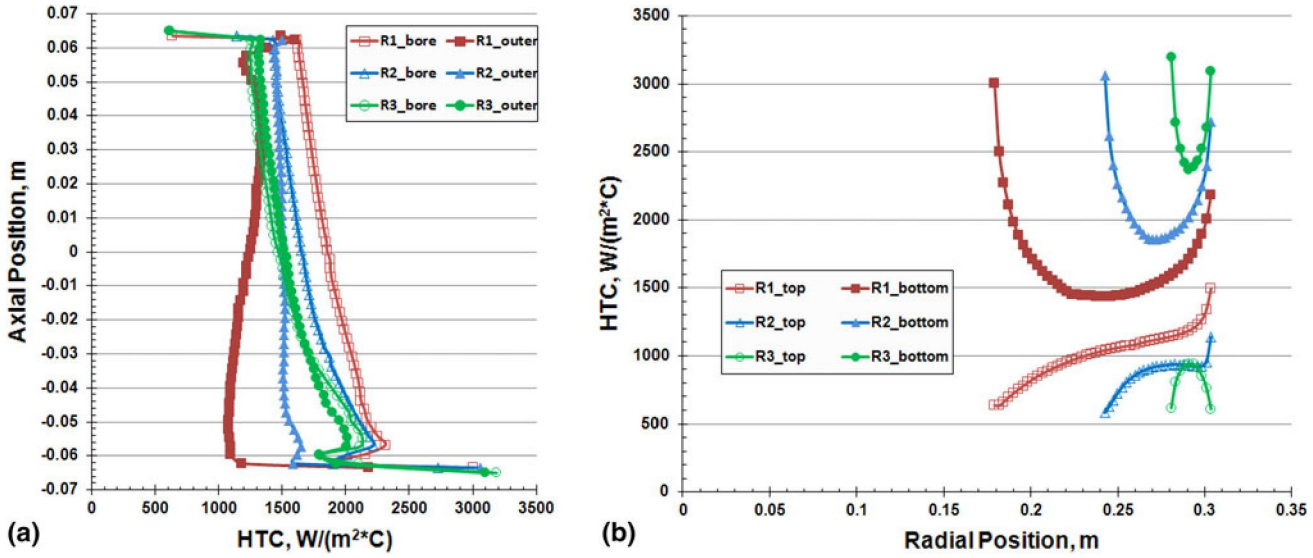

Fig. 5 Average heat-transfer coefficients as a function of position in the three horizontal ring cases. (a) ID and OD values. (b) Bottom and top values for the three rings (Color figure online)

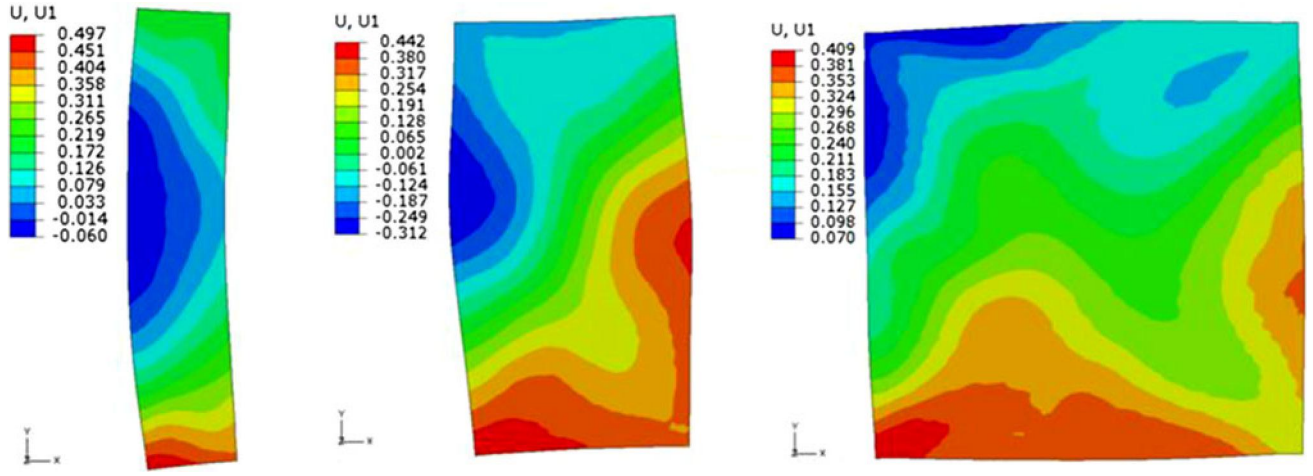

Fig. 6 Predictions of radial displacement for horizontally positioned rings. For each cross section the ID is on the left and OD is on the right (Color figure online)

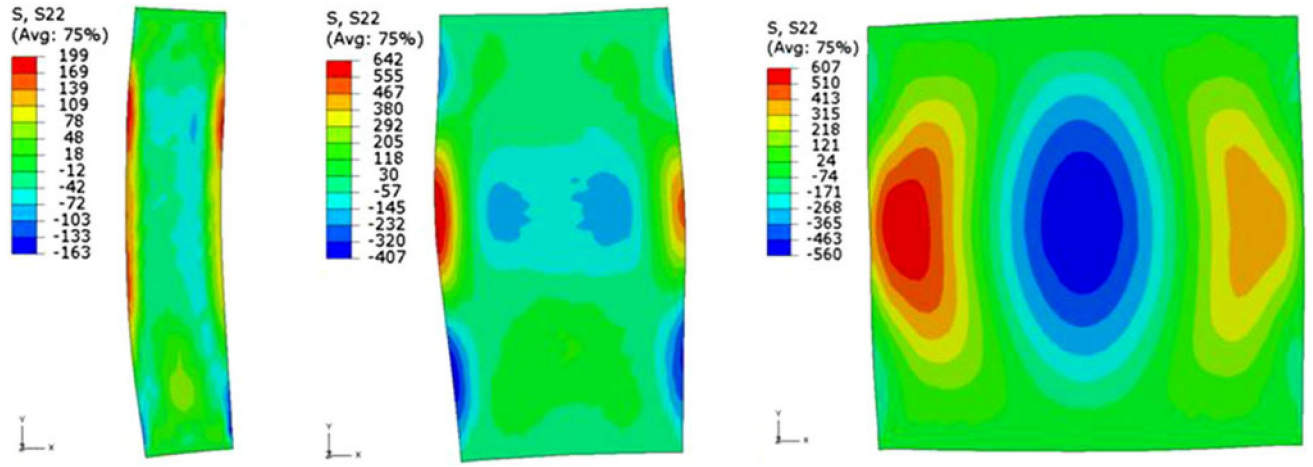

Fig. 7 Predictions of axial stress for horizontally positioned rings. For each cross section, the ID is on the left and OD is on the right (Color figure online)

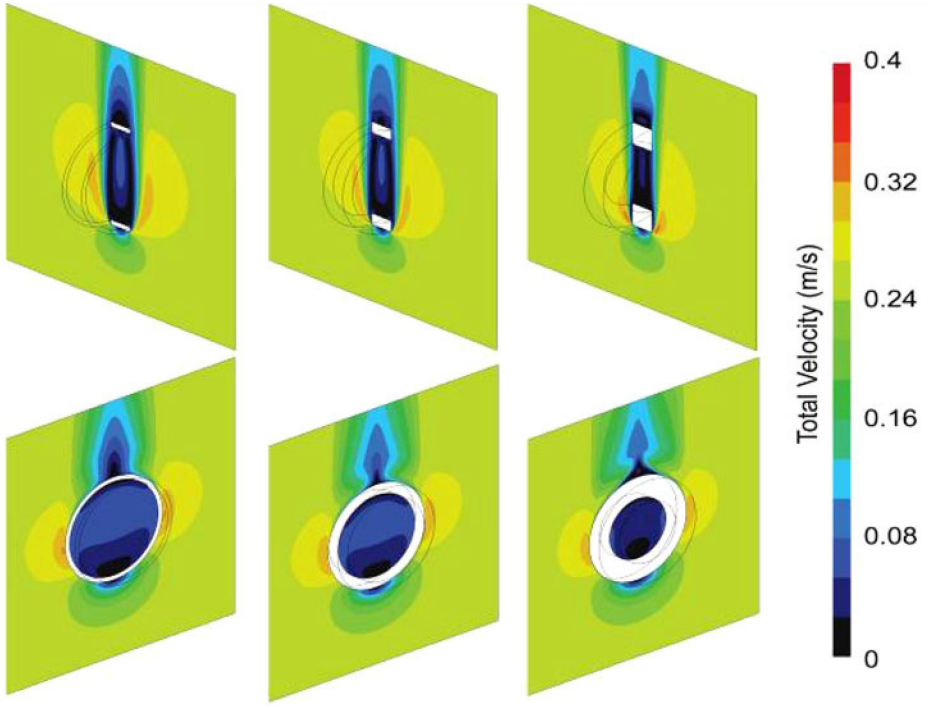

Fig. 8 Flow fields surrounding the three rings with vertical orientation. Ring 3 is at left, Ring 2 is in the middle, and Ring 1 is at the right (Color figure online)

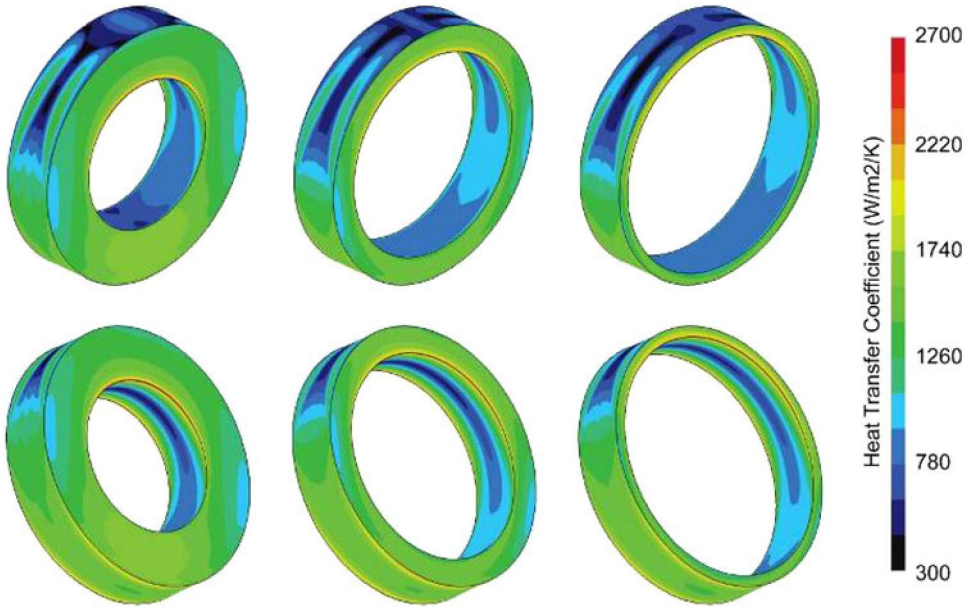

Fig. 9 Resultant heat-transfer coefficients from the flow field with vertical ring orientation. Ring 1 is shown at left, Ring 2 is shown in the middle, and Ring 3 is shown at the right. Flow is from the bottom (Color figure online)

Because of the nonuniformity of heat transfer, both thermal stress and transformation stress are generated. Figure 10 shows predicted axial stress contour plots for the three rings. The axial stress is high for Ring 2 (~750 MPa) and even higher for the thick ring, Ring 1 (~850 MPa). For both Rings 1 and 2, the axial stress is high at mid-height for the entire ID circumference. For the thin ring, Ring 3, the axial stress is nonuniform around the bore, with a peak close to 275 MPa at the "1-2 o'clock position. Axial stress is associated with circumferential cracks.

Hoop stress affects radial cracking on all surfaces. Figure 11 shows the predicted hoop stresses for the bottom and top ring cross sections. For Ring 3 (thin ring), the hoop stresses are relatively low, with the top cross section showing tensile values of about 200 MPa and the bottom cross section having neutral surface stress. Ring 2 has tensile hoop stresses on both the ID

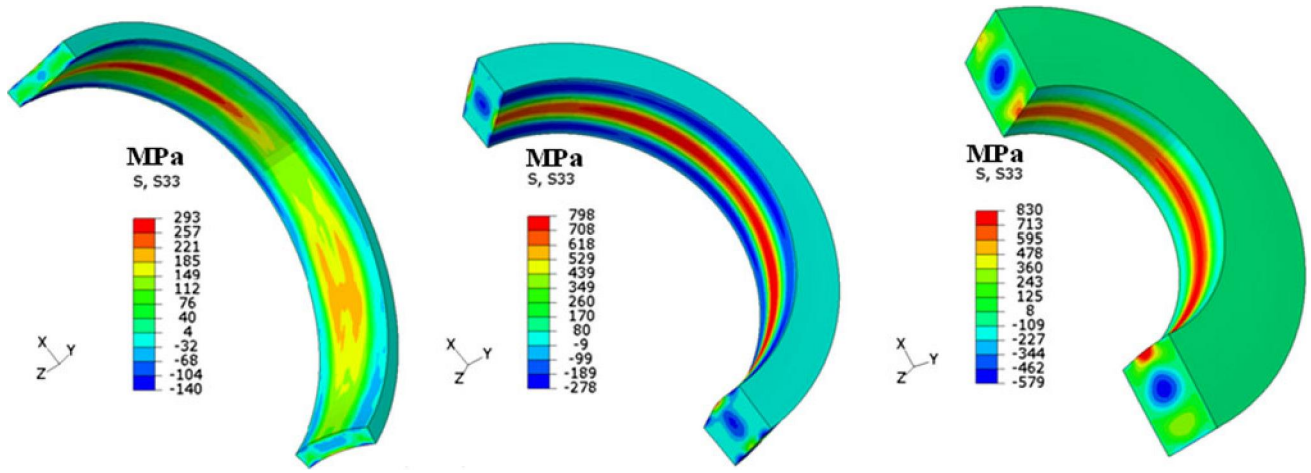

Fig. 10 Stress in the axial direction for quenching vertically positioned rings. The rings have been sectioned to expose the internal stress fields. Flow is in the +X direction (Color figure online)

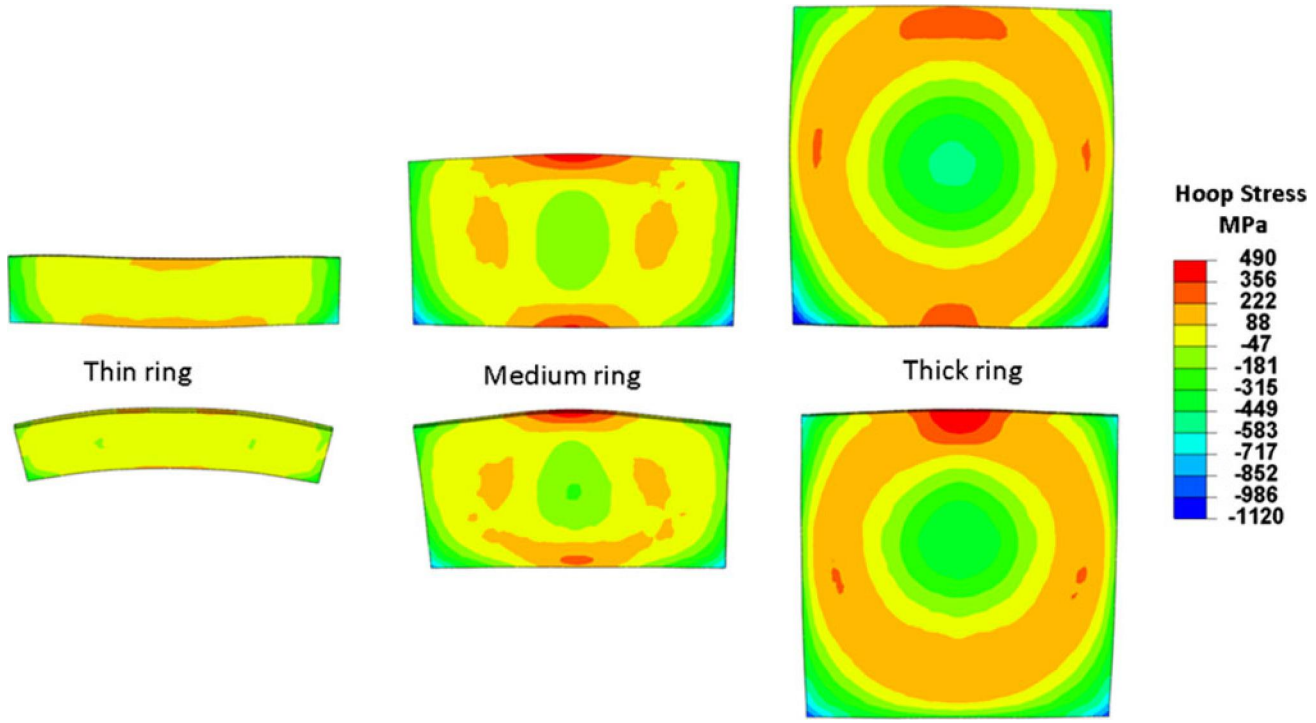

Fig. 11 Hoop stress predictions for the bottom and top cross-sectional locations for the three ring shapes. Shape change is magnified ×10 (Color figure online)

(330 MPa) and OD (475 MPa) surfaces for the top cross section. The bottom location for Ring 2 is predicted to have hoop tension on the ID (400 MPa) and the OD (150 MPa). Interestingly, Ring 1, the thick ring, is predicted to have hoop compression on the bottom OD location (−350 MPa), but tension at the other locations.

Radial displacements around the mid-height circumference of the rings are shown in Fig. 12. For rings 1 and 2 (thick and medium, respectively), growth is predicted, and there is slight ovalling with the vertical direction growing slightly more than the horizontal direction. However, the thin Ring 3, which again hourglasses as shown in Fig. 11, ovality is more of an issue. The vertical axis locations grow, while there is shrinkage at the "4 o'clock position." The nonuniformity of heat transfer has a significant impact on the shape of this thinner ring.

Mention has been made of the effect of the nonuniform heat transfer on phase transformations. Figure 13 shows the final martensite distributions for the rings quenched in the vertical orientation. Ring 3 is nearly 100% martensite due to its thinness and the steel hardenability. Rings 1 and 2 are martensite where heat transfer is relatively high; the side faces are a primary location for high heat transfer. For rings 1 and 2, the heat

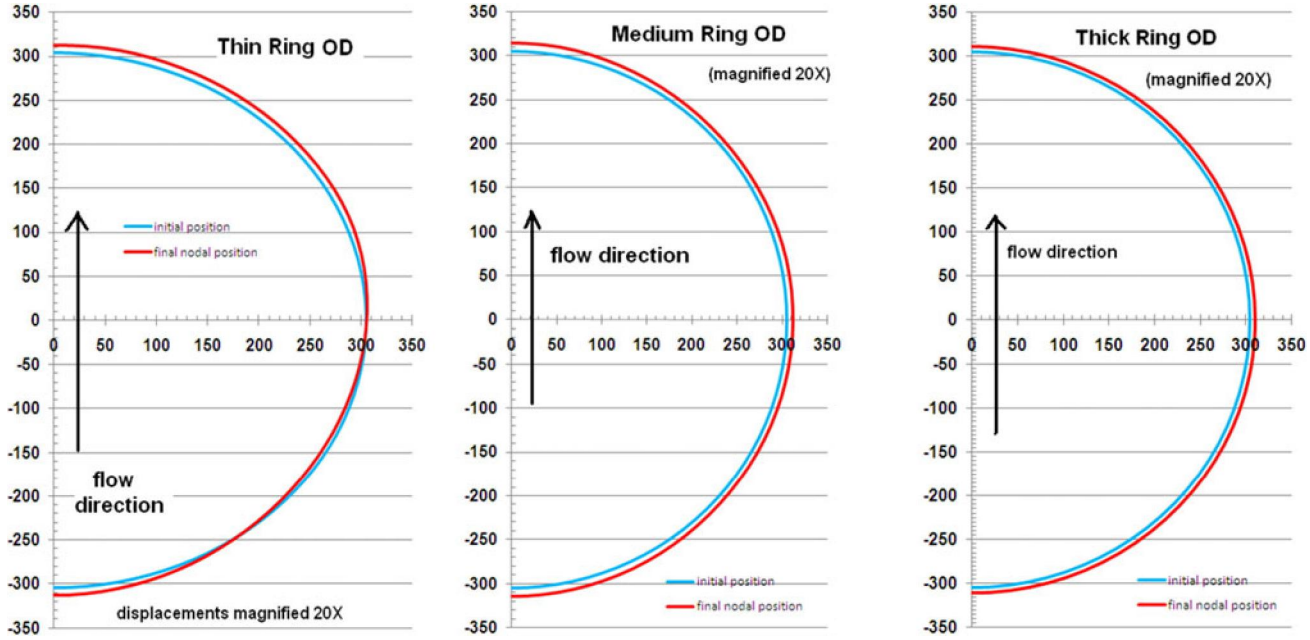

Fig. 12 Radial displacement predictions for the vertical rings (Color figure online)

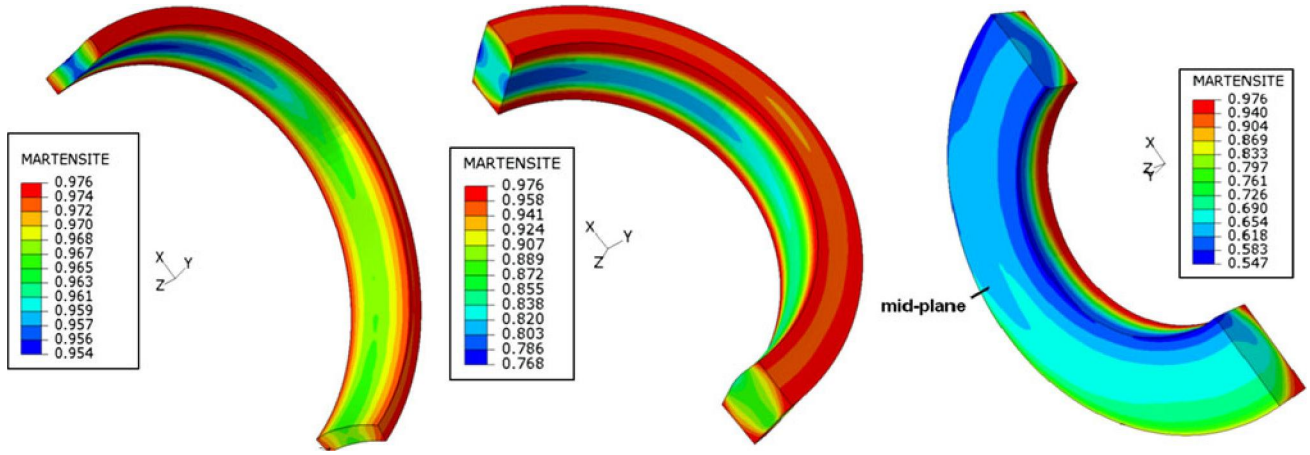

Fig. 13 Final predicted martensite fraction for the three rings quenched in a vertical orientation. The rings have been sectioned to expose the internal martensite distributions. Flow is in the +X direction (Color figure online)

transfer on the ID is lower, and less martensite is formed. The bainite content is 20-25% on the ID of Ring 2 and 30-35% on the ID of Ring 1 around the mid-height location. While Fig. 13 shows the nonuniformity in martensite distribution, it does not show the nonuniformity in the timing of martensite or bainite formation. The timing variation for these transformations plays a significant role in final distortion and residual stress state. Accurate process simulation is especially useful for examining such phase evolution differences.

5. Discussion

Residual stress and distortion are the result of thermally induced stresses and transformation induced stresses. Thermal stresses are the result of nonuniform quenching or heat transfer causing large thermal gradients surface to core, or from surface to surface. Transformational stresses arise from the transformation from austenite to martensite (and to a lesser degree from austenite to bainite). These two sources of residual stresses must be taken into account if distortion and residual stress are to be controlled.

The rolled rings oriented horizontally to the flow all exhibited asymmetric heat transfer between the top and bottom surfaces. As the wall thickness becomes smaller, the differential heat transfer, or average heat extracted becomes more asymmetric. In the case of Ring 1, the average heat extracted is similar, and the average heat extracted out the bottom of the ring is greater by approximately 2:1. In the case of Ring 3, the average heat extracted out of the bottom is an order of magnitude greater. It can be expected that, initially, the bottom surface would shrink, followed by the upper surface shrinking. This would cause a stress reversal in the lower surface. Depending on the magnitude of developed stresses and the stiffness of the ring, in the absence of transformational stresses, it can be expected that a taper would

occur in the ring. It is expected that the taper would be more severe in the thin-walled ring.

The heat transfer on the inner and outer diameter surfaces is similar, but asymmetry exists. As a rule, the outer diameter exhibits a lower overall average heat extraction than does the inner diameter. The average heat extracted difference is smallest for Ring 3 and increases as the wall thickness increases. This local differential heat transfer is greatest approximately 1 cm from the bottom. It is there that the stress field would be the highest. At the upper portion of the rings, there is still a slight difference in the heat extraction; however the differences are negligible.

Ring 3 shows virtually identical heat transfer on the inner and outer surfaces. At the center of the height of Ring 3, the heat extracted on the inner and outer diameters are equal, and the inner surface heat flux rate becomes greater toward the bottom. Interestingly, the inner bore at the top portion of Ring 3 shows lower heat transfer than the outer surface. This is not indicated in the other rings. As the wall thickness increases, the average heat-transfer coefficient on the outside surface decreases, but the average heat-transfer coefficient on the inside bore increases as the wall thickness is increased. This is the result of higher velocities in the inside bore due to Bernoulli effects (i.e., the inner bore acts as a nozzle). However, the bulk heat extracted from the inside and outside diameter surfaces tends to decrease as the wall thickness increases.

Hoop stresses are caused by transformation induced volume changes. For a given alloy hardenability, as the section thickness increases there is reduced transformation to martensite in the center of the ring. Thin wall sections would transform to martensite at approximately the same time, but thicker cross sections would have the interior sections of the wall transform at a later time. It is this transformation to martensite at different times that results in the hoop stresses. The amount of transformation would govern the size of the hoop stress field. At some critical cooling rate, dependent on the alloy, austenite does not transform to martensite, but to upper transformational products. This reduces the volumetric expansion, and would reduce the resultant hoop stresses. This suggests that there is a cooling rate at the center of the ring, faster than the critical cooling rate which would generate the largest hoop stress. This also suggests that an intermediate cross-section would have the greatest propensity to hoop stresses and radial cracking. This is borne out in industrial experience where intermediate sizes, dependant on alloy, have the highest likelihood of radial cracking.

The vertically oriented rings, while having a more complex flow, appear to have a simpler resultant heat transfer (Fig. 9). It is also more consistent between the different ring sizes, regardless of whether it is the side surfaces, inner diameter surface, or the outer diameter surface. There is little difference in the heat transfer around the periphery of the inner diameter surface. In Ring 1, there appears to be a slight reduction in the average heat transfer at the bottom of the inner diameter from wake effects. However, this small amount of decrease is insignificant compared with the overall heat-transfer coefficient.

There is some asymmetry to the heat transfer, with the greatest heat transfer occurring at the top portion of the inner diameter surface. The net difference in the vertical direction is 400 W/(m^2 K).

The outer diameter surface has a similar profile; however, it has the greatest heat transfer at the bottom of the outer diameter surface. This is opposite of the inner diameter. This indicates that the lower and upper portions of the ring have a higher differential heat-transfer coefficient, and have stress fields in opposite directions. Interestingly, they are of approximately the same magnitudes. This nonaxisymmetric heat-transfer between the upper outer diameter and upper inner surfaces of the ring, and the lower outer diameter and the lower inner diameter, would result in buckling similar to a potato chip or hyperbolic paraboloid ("potato chipping") 3. The extent of the distortion would tend to be dependent on the stiffness of the ring, with the thinner wall ring being more prone to twisting. The central bore would also be distorted, with an elongation or "egging" in the vertical direction.

The side surfaces show relatively uniform heat transfer across the rings. Because of this symmetry between the two sides, the relative difference in heat transfer would have little effect on the overall shape.

6. Summary

The purpose of this study was to look at heat-transfer trends during quenching of rings with varied geometry and quenching orientation. The CFD approach was to capture a snapshot in time to determine the fluid flow field around the rings. This was accomplished by solving a static model, and this provided sets of average heat-transfer coefficients that were then used to compare the residual stress states, dimensional changes and final phase fractions for the rings. The authors acknowledge that the use of a single static CFD simulation and average heat-transfer coefficients for the heat-treated simulations do not reflect total reality of actual conditions. Nonetheless, these results provide useful trends in ring behavior.

From this investigation, some basic observations can be made as follows:

Horizontal Orientation:

- Flow is symmetric around ring. As wall thickness decreases, flow attachment at inner diameter wall increases.
- Asymmetric heat flux occurs at top and bottom surfaces. As wall thickness decreases, asymmetry increases, with the average heat extracted increasing by an order of magnitude.
- The inner/outer diameter heat transfer is similar, but asymmetric. As wall thickness increases, the average heat flux on the outside diameter decreases, but the inside diameter average heat flux increases as the diameter increases. A local increase of heat-transfer coefficient occurs approximately 1 cm from the bottom of the ring, which would contribute to a localized stress field.
- Hoop stresses in the rings are the result of transformation induced stresses.

Vertical Orientation:

- Flow fields are much more complex for the vertical orientation but appear to have simpler heat-transfer characteristics.
- The heat transfers between the upper inner and outer diameters, and the lower outer diameter and the lower inner diameters would result in a thermal stress fields with a tensile hoop stress at the upper inner diameter, and a tensile hoop stress at the lower outer diameter, assuming elastic stresses. This stress field would result in a hyperbolic paraboloid ("potato chipping") distortion. The amount of distortion is dependent on the stiffness of the ring. As the wall thickness increases, the amount of distortion decreases. The thin ring

would be the most susceptible to distortion. "Egging" of the bore would also occur in the vertical direction.

Acknowledgments

The authors gratefully acknowledge the support of their companies for this study. Helpful discussions with their colleagues are also gratefully acknowledged.

References

1. Azore® Technologies, LLC, *Azore® Users Guide*, 2011
2. J.D. Franklin and J.S. Lee, Momentum/Continuity Coupling with Large Non-Isotropic Momentum Source Terms, *Int. J. Numer. Methods Fluids*, 2009, **61**, p 946–969
3. J.H. Ferziger and H. Peric, *Computational Methods for Fluid Dynamics*, Springer, New York, 1997
4. Deformation Control Technology, Inc., *DANTE Users Manual*, 2011